Research Square

Preprints are preliminary reports that have not undergone peer review.
They should not be considered conclusive, used to inform clinical practice,
or referenced by the media as validated information.

Spin-Based Quantum Information Processing in Cytoskeletal Filaments Using Nucleoside Phosphates

Robert Trandafir
Carol Davila University of Medicine and Pharmacy
Lea Gassab
University of Waterloo
Travis John Adrian Craddock
travis.craddock@uwaterloo.ca
University of Waterloo

Article

Keywords: quantum information processing, phosphorus-31, nuclear magnetic resonance, cytoskeletal filaments, microtubules, filamentous actin

Posted Date: November 9th, 2026

DOI: https://doi.org/10.21203/rs.3.rs-11393005/v1

License: This work is licensed under a Creative Commons Attribution 4.0 International License.
Read Full License

Additional Declarations: No competing interests reported.

Spin-Based Quantum Information Processing in Cytoskeletal Filaments Using Nucleoside Phosphates

Robert Trandafir[1], **Lea Gassab**[2,3,4,5], **and Travis J.A. Craddock**[2,3,4,*]

[1]Carol Davila University of Medicine and Pharmacy, Bucharest, Romania
[2]Department of Biology, University of Waterloo, Waterloo, ON, Canada
[3]Waterloo Institute for Nanotechnology, University of Waterloo, Waterloo, ON, Canada
[4]Department of Physics & Astronomy, University of Waterloo, Waterloo, ON, Canada
[5]Department of Chemistry, University of Waterloo, Waterloo, ON, Canada
[*]Correspondence: travis.craddock@uwaterloo.ca

ABSTRACT

Phosphorus nuclear spins are candidates for quantum information processing in biological matter because ^{31}P is a spin-1/2 nucleus without an electric quadrupole moment, although coherence remains environment-dependent. Recent work ranges from theoretical proposals based on phosphate ions and Posner molecules to experimental demonstrations of room-temperature quantum logic in adenosine diphosphate. Scaling such approaches in liquid-state molecular systems is difficult because slower rotational dynamics in larger phosphate-containing structures weaken motional averaging, restore anisotropic couplings, broaden spectra, and can reduce transverse coherence. We therefore propose investigating a transition to oriented, immobilized biomolecular architectures. Filamentous actin and microtubules provide ordered lattices containing bound ADP and GDP/GTP, respectively, at periodic nucleotide-binding sites and offer geometries suitable for orientation-dependent NMR studies. Using structural models based on PDB entries 7BT7 and 5SYF, we estimate static intranucleotide ^{31}P–^{31}P dipolar contributions and corresponding conditional two-spin interaction intervals in aligned lattices. The resulting sub-millisecond interaction timescales motivate direct measurements of relaxation, linewidths, orientation dependence, and selective control. Cytoskeletal nucleotide-spin lattices therefore merit investigation as candidate platforms for solid-state nuclear magnetic resonance quantum information processing in biological matter.

Keywords: quantum information processing, phosphorus-31, nuclear magnetic resonance, cytoskeletal filaments, microtubules, filamentous actin

Introduction

A classical bit occupies one of two states, whereas a qubit is a two-level quantum system that can occupy a coherent superposition of its basis states and can be manipulated and measured using suitable control fields. Biological qubits such as enhanced yellow fluorescent protein (EYFP) [1] and the magneto-sensitive fluorescent flavoprotein MagLOV [2], which can be interrogated and externally controlled in living systems, may enable ultrasensitive measurements for fundamental research and medical diagnostics. They may also be integrated into scalable, biocompatible architectures for quantum sensing, information processing, and, ultimately, biological quantum computation.

Among the principal elements of biological matter (carbon, hydrogen, nitrogen, oxygen, phosphorus, and sulfur; CHNOPS), phosphorus has been proposed as a particularly promising host for natural nuclear-spin qubits. Its sole stable isotope, phosphorus-31 (^{31}P), has nuclear spin 1/2 and therefore no electric quadrupole moment, which reduces decoherence from direct coupling to local electric-field gradients. Its 100% natural abundance and widespread occurrence in biological phosphates further support its suitability. Moreover, ^{31}P nuclear spins can be addressed, manipulated, and detected using magnetic and radiofrequency fields, although their coherence depends on the surrounding molecular environment. These properties have motivated several proposals for phosphorus-based quantum information processing in biological systems.

Fisher proposed that solvated phosphate ions could act as entangled qubits in biology with long coherence times and identified calcium phosphate clusters known as Posner molecules as potential structures for retaining quantum information [3] (Fig. 1). In this proposal, phosphorus nuclear spins may first become entangled through biochemical reactions involving phosphate groups from adenosine triphosphate (ATP) or polyphosphate chains (Fig. 1A). Rapid tumbling of solvated Posner molecules was proposed to average time-dependent magnetic interactions, thereby extending coherence and entanglement lifetimes (Fig. 1D). Halpern and Crosson [4] rigorously analyzed this model, validating some aspects while refining the

conditions required for the proposed processes. More recent studies have examined the assumed molecular symmetry [5] and the robustness of coherence and entanglement in Posner molecules [6], but the available work remains primarily theoretical.

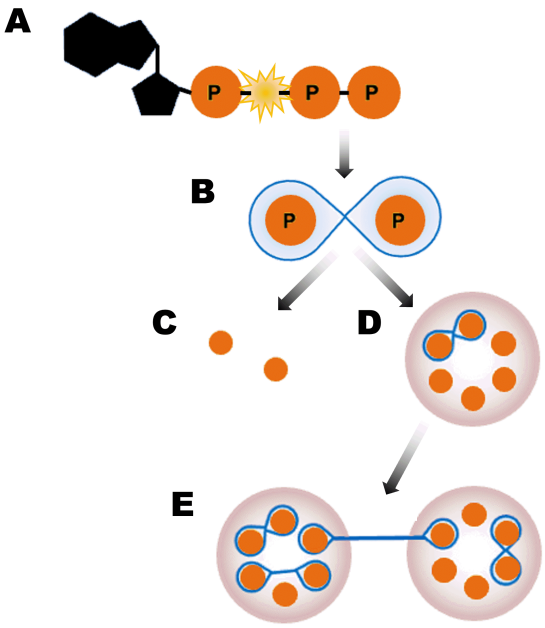


Figure 1. Fisher's spin-based model of quantum cognition. (A) ATP (black) releases pyrophosphate, comprising two linked phosphate groups (orange). (B) The nuclear spins of the two phosphorus atoms become entangled (blue lines). (C) Direct environmental exposure causes rapid decoherence and loss of this entanglement. (D) Incorporation of phosphate into Posner molecules, $Ca_9(PO_4)_6$ (pink), may protect the nuclear-spin states from decoherence. (E) Entanglement may persist between phosphate groups within the same Posner molecule or between separate Posner molecules, potentially enabling quantum correlations over biologically relevant distances.

Smolin proposed another biologically inspired architecture for ^{31}P quantum information processing based on the phospholipid cell membrane [7]. Phospholipids are major components of cell membranes and contain a phosphate head group and two hydrophobic tails (Fig. 2A). Smolin's proposal assumes electron spins associated with selected phospholipids (Fig. 2B). However, phosphatidylcholine is a closed-shell zwitterion under physiological conditions, so its charged phosphate and choline groups do not themselves imply an unpaired electron. An electron-spin control qubit would require a separately generated, sufficiently long-lived radical state, for example through photoexcitation or redox chemistry. Conditional on the generation of such radical states, the proposed lipid-bilayer architecture resembles the Kane quantum-computer design [8] (Fig. 2C). Potential advantages include tunable control-qubit density through the proportion of modified phospholipids and a simpler fabrication process in which an electric field positions the polar lipids in the fluid phase before cooling immobilizes them below the membrane transition temperature.

More recently, Davino experimentally demonstrated quantum information processing on a two-qubit system of phosphorus nuclear spins in adenosine diphosphate (ADP) [9]. Remarkably, the T_2 decoherence time of the nuclear spins was measured to be 207(6) ms, and the CNOT, Hadamard, and T quantum logic gates were implemented with fidelities of 0.970(53), 0.991(55), and 0.918(70), respectively. These gates, together with standard rotation gates, form a universal gate set. In the same ADP study, effective Bell-state preparation and a proof-of-principle implementation of the Deutsch algorithm were demonstrated [9]; Refs. [10–13] provide background on ensemble-NMR effective-pure-state methods, and Ref. [14] introduced the Deutsch algorithm.

Although these results establish room-temperature quantum control in a biologically relevant molecule, scaling remains difficult. ATP would constitute a three-qubit system described by an 8×8 density matrix. This size is tractable, but state preparation, spectral resolution, pulse design, and tomography become progressively more demanding.

Still, running complex quantum algorithms (such as the Deutsch–Jozsa algorithm [15]) would require many more qubits, and a possible solution has been suggested in [9]: using long-chain polyphosphates, which are present in living systems [16]. However, beyond the practical challenge of spectral overcrowding, a fundamental physical constraint arises from the scaling of molecular dynamics. The high-field secular approximation is distinct from motional averaging: rapid molecular tumbling

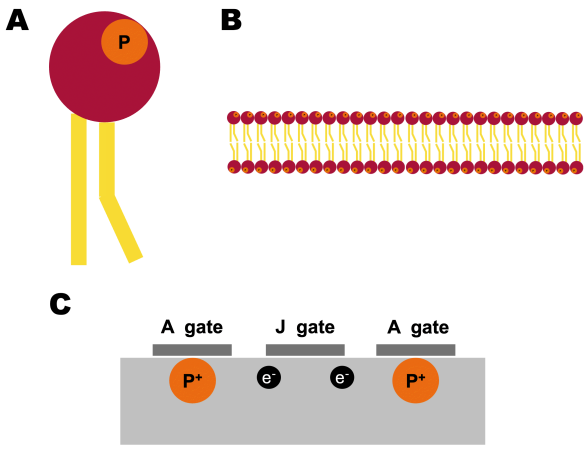


Figure 2. Smolin's proposed phospholipid implementation of a Kane-type quantum computer. (A) Schematic phospholipid comprising a phosphorus (orange)-containing polar headgroup (red) and two hydrophobic acyl chains (yellow). (B) Organization of phospholipids into a bilayer, producing a two-dimensional array of ^{31}P nuclear spins that may serve as memory qubits. (C) Conceptual Kane-type architecture in which unpaired electron spins (e^-; black) associated with selected phospholipids act as control qubits. Local A gates tune the coupling between an electron spin and a neighboring ^{31}P nuclear spin, whereas the intervening J gate controls the interaction between adjacent electron spins.

averages orientation-dependent anisotropic interactions in solution, whereas the secular approximation removes terms that oscillate rapidly relative to the Zeeman dynamics.

For polyphosphate chains containing hundreds of phosphorus atoms, the rotational correlation time (τ_c), defined as the characteristic timescale of molecular tumbling, would increase substantially. In the Bloembergen-Purcell-Pound (BPP) framework, τ_c scales approximately with the cube of the hydrodynamic radius (a^3). Slower tumbling weakens motional averaging and restores anisotropic coupling contributions, causing line broadening and potentially reducing the transverse coherence time T_2.

Increasing the qubit count may require an oriented, immobilized solid-state regime, and cytoskeletal filaments provide candidate biomolecular lattices for investigating this possibility. Actin filaments are one of the three major types of cytoskeletal filaments, and actin is among the most abundant proteins in eukaryotic cells [17]. F-actin consists of two intertwined strands, with approximately 13 globular actin monomers repeating over six turns and an axial repeat of 35.9 nm [18]. Using PyMOL and the Protein Data Bank (PDB) structure 7BT7 of the F-actin-ADP complex [19], we measured approximately 4.0 nm between adjacent ADP sites. This estimate is consistent with the deposited 7BT7 helical symmetry, which has an axial rise of 2.75 nm and a rotation of -166.6° per subunit. These lattices provide candidate solid-state structures beyond solution-state ADP, where filamentous actin sterically constrains bound nucleotides within its subunits, allowing static, orientation-dependent dipole-dipole coupling between phosphorus nuclear spins.

Microtubules are another central component of the cytoskeleton and are composed of alpha and beta tubulin heterodimers in which alpha-tubulin binds guanosine triphosphate (GTP) at a non-exchangeable, non-hydrolyzable N-site while beta-tubulin binds GTP at an exchangeable E-site, where the bound GTP is hydrolyzed to guanosine diphosphate (GDP) shortly after tubulin incorporation into the growing microtubule polymer. They are assembled from these tubulin subunits into long hollow polymers that are 25 nm wide and range in length from 1 to 100 micrometers. Microtubule structure is most straightforwardly described as comprising approximately 13 linear protofilaments that are associated laterally and closed into a hollow tube.

Along with microtubule-associated proteins, they form the mitotic spindle, essential in separating the chromosomes during mitosis, a central process in cell biology [20]. Microtubules also play major roles in cellular organization and in intracellular transport, crucial for processes associated with long axons of neurons, such as neurotransmitter release and synaptic plasticity [21].

Cytoskeletal filaments are attractive candidate hosts because they form ordered lattices of regularly spaced molecules over micrometre length scales, a potentially useful feature for solid-state nuclear magnetic resonance (NMR) quantum-information devices. In microtubules, proposed advantages include their geometry, hydrophobic pockets, high density of aromatic amino acids, and ordered internal water, although any resulting protection from environmental noise or enhancement of coherence must be demonstrated experimentally [22–25]. Filamentous actin may partly shield bound nucleotide phosphates from bulk solvent, but its effect on ^{31}P relaxation and coherence must also be measured directly. Beyond the present ^{31}P nuclear-spin proposal, microtubules have been proposed to support room-temperature exciton formation and transport [26] and strongly superradiant

states [27–30]. These theoretical quantum-optical proposals, together with the established biological functions of cytoskeletal filaments, motivate further investigation. Microtubules contribute to neuronal organization and plasticity [31,32], whereas actin contributes to cell motility [33], muscle contraction [34], cell division [35], phagocytosis [36], antigen presentation [37], and the immunological synapse [38].

We propose investigating phosphorus nuclear spins in nucleotides periodically embedded in F-actin and microtubule lattices as candidate solid-state NMR qubits. Quantum biology has commonly encompassed two broad areas: (i) the study of nontrivial quantum effects in biological systems and (ii) the use of quantum-enabled techniques, such as quantum dots [39], nitrogen-vacancy centers in diamond [40,41], and fluorescence lifetime imaging microscopy [42], to investigate biological processes with high spatial and temporal resolution.

It might also be worth considering a third area: the use of biomolecular architectures as hardware for quantum information processing devices. Biology may offer useful design principles for operation in noisy environments, and noise-assisted effects can enhance specific transport or computational processes [43–45]; however, such effects are not equivalent to fault-tolerant quantum computation, which requires explicit error-detection and correction mechanisms.

Biomolecular self-assembly may reduce some lattice-fabrication burdens, although purification, isotope engineering, alignment, stabilization, control, and readout remain substantial challenges. Because these lattices are built from repeated subunits and extend over micrometre length scales, they also offer a possible route to dense spin networks without atom-by-atom placement. In principle, such structures could support richer coupling geometries than isolated small molecules, although useful qubit number and connectivity would still depend on spectral distinguishability and selective control.

If the required control and scalability conditions can be met, biomolecular quantum hardware could eventually contribute to algorithms relevant to bioinformatics [46], molecular biology [47], genomics [48], oncology [49–53], drug design and discovery [54–56], drug-response prediction [57], cell-based therapeutics [58], and precision medicine [59, 60]. These applications remain long-term motivations rather than demonstrated capabilities of the present architecture.

Results

For the intranucleotide P_α–P_β pair considered here, define the effective coupling in Hz as $J_{12}^{\mathrm{eff}}/(2\pi) = J_{12} + D_{12}/(2\pi)$. The characteristic two-spin interaction interval is $t_{\mathrm{int}} = 1/[2|J_{12}^{\mathrm{eff}}/(2\pi)|]$. We use $J_{12} = 22.7$ Hz from solution-state ADP [9] only as a provisional approximation; direct measurement or electronic-structure calculation is required for nucleotide phosphates bound in actin and tubulin because the local environment and Mg^{2+} coordination may change J_{12}.

Because 7BT7 and 5SYF are cryo-EM coordinate models reported at resolutions of 3.80 Å and 3.50 Å, respectively, the nucleotide P–P distances, orientation angles, and derived dipolar couplings reported below should be interpreted as deterministic estimates from the deposited/refined coordinate models. The displayed numerical digits reflect the coordinate calculations and should not be interpreted as experimental coordinate precision.

With the convention of equations (2), (4), and (5), $D_{12} = [\mu_0\gamma^2\hbar/(4\pi r^3)](1 - 3\cos^2\theta)$ is in rad s^{-1}; equivalently, $D_{12}/(2\pi) = [\mu_0\gamma^2\hbar/(8\pi^2 r^3)](1 - 3\cos^2\theta)$ is in Hz. For F-actin, the coordinate-based inputs are $r = 2.7737$ Å and $\theta = 99.5377^\circ$. Using one global B_0 axis gives $D_{12}/(2\pi) = 846.39$ Hz. Therefore, $J_{12}^{\mathrm{eff}}/(2\pi) = 22.7$ Hz $+846.39$ Hz $= 869.09$ Hz. The corresponding interaction interval is $1/[2(869.09\ \mathrm{Hz})] = 0.5753$ ms, about 38.3 times shorter than the liquid-state value. This is an interaction timescale, not a demonstrated gate time.

As a coordinate-model variability check, we also evaluated the five ADP molecules directly present in the deposited 7BT7 model. Their modeled P_α–P_β distances range from 2.7659 to 2.7779 Å, whereas the modeled angle between the P–P vector and the global filament axis ranges from 99.5377° to 142.4920°. Applied directly, these deposited coordinates yield $D_{12}/(2\pi)$ values ranging from -825.87 to 846.39 Hz and corresponding interaction intervals of 0.5753–0.6400 ms. These differences are treated as variability among deposited/refined ligand coordinates rather than as experimentally resolved conformational heterogeneity. The main model instead uses the Chain A ADP geometry repeated according to the ideal 7BT7 helical symmetry described above.

For the microtubule model, the coordinate-based inputs are $r = 2.8352$ Å and $\theta = 104.5867^\circ$. Across the 26 symmetry-generated GDP copies, the P–P distance and the angle to the global microtubule axis are invariant under the rigid-body biological-assembly transformations apart from floating-point roundoff; this numerical invariance does not represent sub-Å or sub-degree experimental precision. Using one global B_0 axis gives $D_{12}/(2\pi) = 699.33$ Hz and $J_{12}^{\mathrm{eff}}/(2\pi) = 699.33$ Hz $+22.7$ Hz $= 722.03$ Hz. The corresponding interaction interval is $1/[2(722.03\ \mathrm{Hz})] = 0.6925$ ms, about 31.8 times shorter than the liquid-state value. This estimate remains conditional on the structural orientation and weak-coupling assumptions.

Cytoskeletal nucleotide pockets may have relaxation properties distinct from those of conventional rigid solids because of local dynamics, partial solvent shielding, proton density, and Mg^{2+} coordination [70–72]. These features do not by themselves establish longer coherence or protection analogous to that proposed for doped Posner molecules [3,4,73–75]. Instead, they motivate direct measurements of T_1, T_2, linewidths, and orientation dependence in aligned F-actin and microtubule samples. If

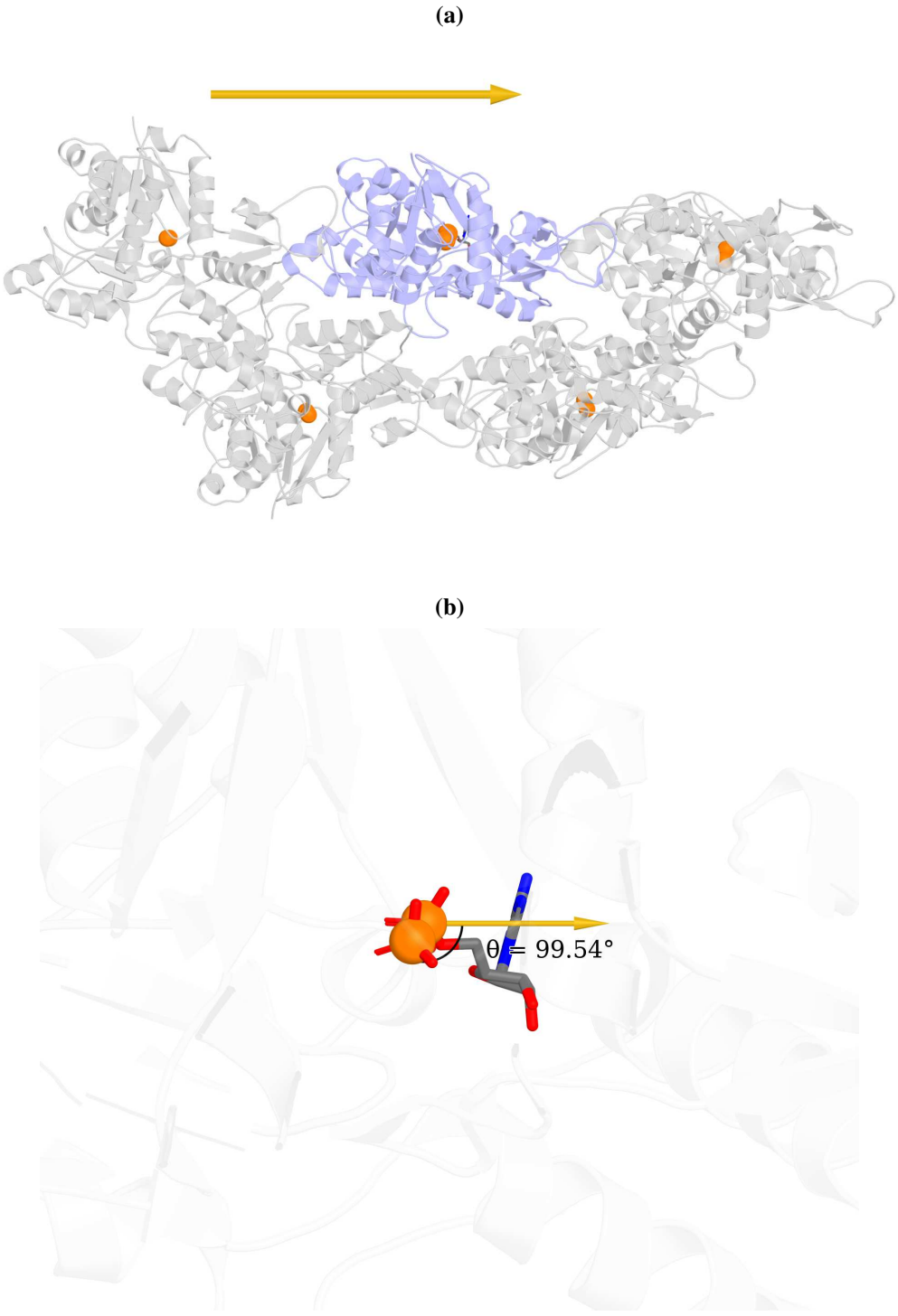


Figure 3. F-actin phosphorus-spin geometry. (a) Idealized F-actin segment generated from the Chain A protomer of PDB 7BT7 using the helical symmetry of the deposited reconstruction (27.5 Å axial rise and -166.6° rotation per subunit). The reference protomer is shown in light blue, the symmetry-generated protomers in gray, and the repeated ADP P_α/P_β sites as orange spheres. The gold arrow indicates the global magnetic-field direction B_0, aligned with the global filament axis obtained from the deposited 7BT7 coordinates. (b) Close-up of the reference ADP showing the P_α–P_β geometry and the angle $\theta = 99.54^\circ$ relative to B_0.

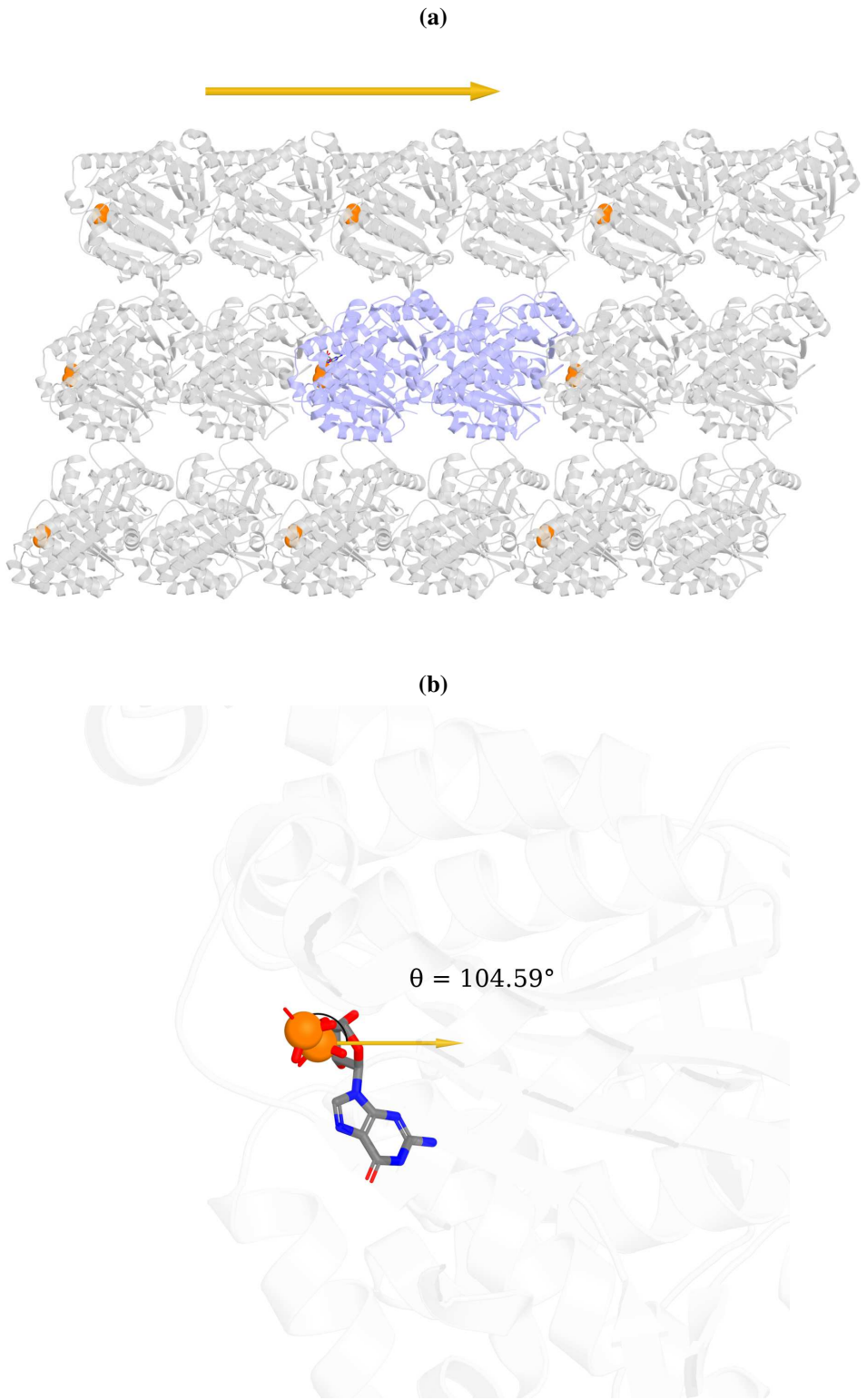


Figure 4. Microtubule phosphorus-spin geometry. (a) Representative 3×3 microtubule wall patch comprising three neighboring protofilaments and three axial tubulin-dimer repeats. The reference α/β-tubulin heterodimer is shown in light blue, the remaining dimers in gray, and the repeated GDP P_α/P_β sites as orange spheres. The gold arrow indicates B_0, aligned with the microtubule axis. The displayed patch is for visualization; coordinate validation used all 26 symmetry operations of the 5SYF biological assembly. (b) Close-up of the reference GDP showing the P_α–P_β geometry and the angle $\theta = 104.59°$ relative to B_0.

direct measurements reveal favorable relaxation behavior in these pockets, local shielding and coordination could become a practical coherence advantage of the biomolecular host; at present this remains a testable hypothesis.

Discussion

Building on these ideas, in his dissertation under the supervision of Vesna Mitrovic, Donovan Davino modeled ADP as a two-qubit ^{31}P nuclear spin system linked by J-coupling.

Davino developed an NMR framework for qubit control, effective Bell-state preparation, quantum-gate operations, and a proof-of-principle Deutsch-algorithm implementation in ADP. The reported ^{31}P transverse coherence time was 207 ± 6 ms, with room-temperature gate fidelities of approximately 97% for a CNOT gate, 99% for a Hadamard gate, and 92% for T gate [9, 73, 76]. These results establish control in solution-state ADP but do not demonstrate operation at physiological temperature or scalability to a cytoskeletal lattice.

Directly scaling the liquid-state proposals becomes increasingly difficult because of spectral crowding, anisotropic couplings, and reduced coherence in large molecules. Larger architectures may therefore require structured phosphorus lattices with fixed qubit geometries.

As such, we propose cytoskeletal filaments as candidate ordered hosts for solid-state quantum-computing architectures based on ^{31}P nuclear spins in GDP/GTP and ADP/ATP. The choice of microtubules and actin as structural hosts was primarily motivated by their regularly spaced lattices of GDP/GTP and ADP/ATP, respectively, and by their critical roles in biological functions, ranging from subcellular activities—such as intracellular transport, establishing cell polarity, and cell division—to organism-level processes, including tissue-level dynamics underlying morphogenesis and neuronal connectivity, which contribute to sensorimotor integration, cognition, and adaptive interactions between organisms and their environments.

We applied the high-field NMR secular approximation [61, 62] and introduced the BPP theory as a phenomenological framework for exploring relaxation as a function of local correlation time [77].

Using the coordinate-based structural orientations gives characteristic two-spin interaction intervals of 0.6925 ms for microtubules and 0.5753 ms for F-actin. These are conditional Hamiltonian timescales, not experimentally demonstrated gate times; pulse, relaxation, orientation-disorder, and readout simulations are still required.

The current architecture employs ensemble readout, consistent with established nuclear magnetic resonance (NMR) methodologies. Consequently, the detected signal represents a population average. Population averaging does not itself provide spectral resolution; the alpha- and beta-phosphate resonances may be separated by their distinct chemical shifts.

In its simplest ensemble-NMR form, this architecture is not scalable in the conventional sense of individually addressable qubits. It is limited to two addressable qubits for ADP/GDP or three for ATP/GTP, which is sufficient only for elementary quantum algorithms. Increasing the qubit count would require additional spectrally distinguishable spin environments and selective control.

A particularly appealing approach would be to "barcode" different classes of GDP molecules by separating their resonances in the frequency domain so that they could be addressed (i.e., initialized, manipulated, and read out) individually. As a rough estimate, the frequency separation would need to be significantly greater than the coupling magnitude (which in our case is 722.03 Hz).

If the alpha- and beta-phosphate resonances remain sufficiently separated in the cytoskeletal environment, their distinct chemical shifts could permit separate control. Modifying the local electronic environment of the phosphorus nuclei may therefore provide a route toward increasing qubit addressability.

Reference [31] proposed a model in which CaMKII-mediated tubulin phosphorylation could contribute to microtubule-based information storage and processing. Building on that hypothesis, we consider whether phosphorylation near the nucleotide-binding region could alter the local ^{31}P magnetic environment. One candidate site discussed in [31] is threonine 312, located in the cleft between the alpha- and beta-tubulin monomers; however, the exact CaMKII phosphorylation site or sites on tubulin remain uncertain. If T312 or another nearby residue is phosphorylated, the resulting electrostatic perturbation could affect nucleotide ^{31}P chemical shifts. Determining whether this occurs will require structural modeling and ^{31}P NMR chemical-shift calculations.

Another PTM that could significantly affect the resonance frequency is polyamination of beta-tubulin at glutamine 15, a primary polyamination site located close to the hydrolysable GTP-binding pocket [78]. Its effect could be comparable to that of a divalent cation such as Mg^{2+}, which produces a shift of about 2 ppm according to [79]. At 11.75 T, a 2 ppm ^{31}P chemical-shift change corresponds to approximately 405 Hz [79]. This is smaller than the coordinate-based 722.03 Hz effective coupling and therefore does not by itself establish selective addressability.

Actin also undergoes post-translational modifications including phosphorylation and redox-dependent oxidation that regulate its structure and dynamics [80–82]. Although the best-characterized redox-sensitive residues (e.g., Cys374 and Met44) are not located within the nucleotide-binding cleft, PTMs occurring at or structurally coupled to this region could plausibly alter local electrostatics and conformational dynamics surrounding the bound ATP or ADP molecule. Such perturbations may modify the

electronic shielding of the nucleotide ^{31}P nuclei and, if accompanied by small structural rearrangements, influence effective spin–spin couplings. While this mechanism remains hypothetical, it provides a biologically plausible route by which naturally occurring PTMs could modulate the local magnetic environment of nucleotide-associated nuclear spins.

Kane-type donor-spin architectures require precise host-crystal engineering through methods such as isotopic purification of silicon, donor placement, and atomic-scale lithography; these requirements should not be generalized to every solid-state NMR architecture.

Fabricating donor-spin devices can be challenging because atomic-scale donor placement and defect suppression are not perfectly deterministic. Multiple cycles of lithography, ion implantation, annealing, and post-fabrication characterization may therefore reduce yield and increase resource requirements. These constraints apply most directly to donor-based semiconductor architectures and should not be generalized to all solid-state NMR platforms.

A potential advantage of biomolecular hosts is bottom-up self-assembly, which may reduce some lattice-fabrication requirements but does not remove the costs of purification, isotope engineering, alignment, stabilization, control, and readout.

For example, microtubules self-assemble from alpha- and beta-tubulin subunits at physiological temperature. Tubulin, GTP, magnesium, and buffer components are widely available, and microtubule polymerization can be performed in molecular biology and biophysics laboratories using established protocols [83]. Similarly, globular actin can be assembled into filament gels that can be aligned [63]. Microtubules can also be aligned along a preferred direction [65], providing the macroscopic order needed to orient nuclear spins relative to the external magnetic field in solid-state NMR experiments.

Although biomolecular self-assembly may offer manufacturing advantages, sample preparation remains nontrivial. Robust protocols must ensure filament alignment and stability, accurate characterization of nucleotide occupancy and isotopic composition, and reproducible sample preparation. Relative to donor-placement architectures, the lattice itself is generated in parallel by biological self-assembly, potentially allowing large numbers of periodically positioned nucleotide sites to be produced without atom-by-atom fabrication. This structural scaling would still need to be converted into spectrally distinguishable, controllable qubits.

Among the many future directions, experimentally testing the feasibility of these systems is crucial. For coherence times to be long enough to support quantum information processing in biological environments, the experimental setup requires careful design, including isotopic purification and geometric optimization of the lattices, as well as appropriate quantum-control interventions. Among these, dynamical decoupling techniques, such as robust multi-axis XY-family sequences [84] and concatenated dynamical decoupling sequences [85], might provide a robust framework to suppress the effects of low-frequency environmental noise, significantly prolonging the transverse coherence time T_2 [86–88].

Another possible direction is to interface nitrogen-vacancy (NV) centers in diamond with cytoskeletal architectures. NV centers have applications in quantum information processing [89–92], quantum error correction [93], quantum communication [94], and quantum metrology [95–97]. Near-surface NV centers could potentially sense local magnetic fields from nearby ^{31}P ensembles. However, single-site initialization, manipulation, and readout throughout a cytoskeletal filament have not been demonstrated. The required sensing depth, sensitivity, spectral resolution, field gradients, and effects of coupling to the sample must be quantified.

Such an approach would directly address the recent calls for a bidirectional exchange between quantum biology and quantum technologies [73,76]. The proposed framework combines a self-assembled nuclear-spin host with a possible NV-based sensing interface. It does not directly replace silicon-based architectures or remove the requirements for selective control, initialization, decoupling, and scalable readout. If sufficiently sensitive and selective, such an interface could provide a route toward external readout of increasingly complex spin networks while retaining the self-assembled biomolecular host.

The periodicity and self-assembly of cytoskeletal filaments may reduce some lattice-fabrication burdens but introduce distinct challenges in biomolecular preparation, stability, orientation, coherence, and device integration. These requirements must be demonstrated experimentally before cytoskeletal nucleotide-spin lattices can be considered viable platforms for scalable quantum information processing.

Methods

Reference [9] demonstrated high-fidelity quantum information processing using nucleotide phosphates. Given the similarities between the ^{31}P NMR spectra of ATP and GTP, we use a common formalism to model both cytoskeletal systems.

Spin Hamiltonian and Decoherence Model for Nucleoside Phosphates in Cytoskeletal Lattices

We express Hamiltonians in angular-frequency units ($H/\hbar$): ω and $\Delta\omega$ are in rad s^{-1}, whereas J is in Hz. For ADP in solution, the effective two-spin Hamiltonian is obtained by (i) starting from the Zeeman, scalar J-coupling, and dipole-dipole terms; (ii) removing the anisotropic dipolar interaction through motional averaging in an isotropic liquid; and (iii) applying the secular approximation with respect to the Zeeman term. This gives the effective Hamiltonian:

$$\hat{H}_{\mathrm{Davino}} = \sum_{i=1}^{2} \Delta\omega_i \hat{I}_i^z + 2\pi J_{12} \hat{I}_1^z \hat{I}_2^z. \tag{1}$$

For ADP/ATP and GDP/GTP bound in the nucleotide-binding site of actin and the E-site of tubulin, we consider the aligned, effectively immobilized lattice limit in which whole-nucleotide isotropic tumbling does not average the static dipolar interaction to zero. Residual field fluctuations may arise from local motions in the binding pocket, including librations, side-chain motions, water exchange, and actin or microtubule dynamics.

We retain the structure of equation (1) while (i) including the static dipolar interaction in the Hamiltonian and (ii) reinterpreting the BPP correlation time τ_c as a local correlation time within the nucleotide-binding pocket.

Spin Hamiltonian and secular approximation

We consider N relevant spin-1/2 nuclei (e.g., the phosphorus spins of ADP/ATP or GDP/GTP) with Zeeman frequencies ω_i in a magnetic field B_0. After applying the high-field secular approximation to the dipolar interaction, but before the additional weak-coupling truncation that removes off-resonant flip-flop terms, the Hamiltonian is:

$$\hat{H} = \sum_{i=1}^{N} \omega_i \hat{I}_i^z + 2\pi \sum_{i<j} J_{ij} \hat{\mathbf{I}}_i \cdot \hat{\mathbf{I}}_j + \sum_{i<j} d_{ij} \left(3\hat{I}_i^z \hat{I}_j^z - \hat{\mathbf{I}}_i \cdot \hat{\mathbf{I}}_j \right). \tag{2}$$

where J_{ij} is the scalar coupling in Hz and $d_{ij} = (\mu_0/8\pi)(\gamma_i \gamma_j \hbar / r_{ij}^3)(1 - 3\cos^2\theta_{ij})$ is the secular dipolar coefficient in rad s^{-1}. In contrast to the solution case, we do not invoke motional averaging to set $d_{ij} \to 0$.

We now split $H = H_z + V$, with $H_z = \sum_i \omega_i \hat{I}_i^z$, and treat V as a perturbation. In the interaction picture with respect to H_z, the operator components relevant to the high-field and weak-coupling truncations pick up phases:

$$\hat{I}_i^z \hat{I}_j^z \to \hat{I}_i^z \hat{I}_j^z, \qquad (\Omega = 0), \tag{3a}$$

$$\hat{I}_i^+ \hat{I}_j^- \to \hat{I}_i^+ \hat{I}_j^- \exp[+i(\omega_i - \omega_j)t], \tag{3b}$$

$$\hat{I}_i^+ \hat{I}_j^+ \to \hat{I}_i^+ \hat{I}_j^+ \exp[+i(\omega_i + \omega_j)t], \tag{3c}$$

$$\left|\omega_i - \omega_j\right| \gg \left|2\pi J_{ij}\right|, \left|d_{ij}\right|. \tag{3d}$$

Equations (3a) and (3b) show the interaction-picture phase evolution of terms retained in equation (2). Equation (3c) is included only to display the double-quantum phase removed by the preceding high-field secular approximation; such terms are not present in equation (2). The Hermitian-conjugate terms transform analogously. For the additional weak-coupling approximation, we require equation (3d).

Under equation (3d), zero-quantum flip-flop terms oscillate much faster than the coupling timescales and may be discarded. The high-field approximation separately removes double-quantum terms oscillating at frequencies near $\omega_i + \omega_j$. As a result, all zz-terms ($\hat{I}_i^z \hat{I}_j^z$) are kept, since they commute with H_z and do not oscillate, and double-quantum terms are dropped at high field, whereas flip-flop terms are dropped only when equation (3d) is satisfied.

These are the high-field and additional weak-coupling approximations; see, e.g., Abragam [61] or Slichter [62]. Whether this weak-coupling condition is satisfied for nucleotide phosphates bound in F-actin and microtubules remains to be established experimentally or by chemical-shift calculations; the Ising-only interaction times reported below are therefore conditional on this regime.

After both approximations, the resulting effective Hamiltonian can be written as:

$$\hat{H}_{\mathrm{MT}} = \sum_{i=1}^{N} \Delta\omega_i \hat{I}_i^z + \sum_{i<j} J_{ij}^{\mathrm{eff}} \hat{I}_i^z \hat{I}_j^z, \tag{4}$$

with

$$J_{ij}^{\mathrm{eff}} = 2\pi J_{ij} + D_{ij}. \tag{5}$$

Here D_{ij} is the Ising dipolar coefficient in angular-frequency units (rad s^{-1}), related to equation (2) by $D_{ij} = 2d_{ij}$ and determined by the fixed internuclear distance and angle between the P–P vector and B_0.

Comparing equations (1) and (4), the structure is the same (Zeeman plus an Ising-type $\hat{I}_i^z \hat{I}_j^z$ coupling), but in our case the effective coupling J_{ij}^{eff} explicitly includes the static dipolar contribution D_{ij} that is absent in the liquid-state Hamiltonian as in the ADP solution experiments [9].

To calculate the secular static dipolar coupling D_{12}, we used the 7BT7 PDB structure of the F-actin–ADP complex and performed a coordinate-based helical-axis calculation. The global actin-filament axis was obtained by determining the screw axis of the rigid-body transformations relating the deposited actin subunits A–E. The axial translation and rotation were evaluated for the successive subunit transformations, and their mean and standard deviation are reported below. This single fitted screw axis was then aligned with the laboratory z axis and with B_0, as can be achieved experimentally [63]. The coordinate-based fit to the deposited chains A–E gave an axial rise of 27.490 ± 0.022 Å and a rotation of $-166.690 \pm 0.069^\circ$ per subunit, consistent with the helical symmetry of the deposited 7BT7 reconstruction (27.5 Å axial rise and -166.6° rotation per subunit). The distance between the alpha- and beta-phosphorus atoms and the angle between the P–P vector and this single global B_0 direction were then calculated from the coordinates. For the ideal symmetry model used for the main comparison, Chain A ADP 402 was taken as the reference and symmetry-related copies were generated using the deposited 7BT7 helical-symmetry parameters of 27.5 Å axial rise and -166.6° rotation per subunit.

We next examined whether phosphorus nuclear spins in GDP molecules embedded in a microtubule lattice could be modeled for quantum information processing in the same way as those in filamentous actin. To calculate D_{12}, we used the 5SYF Protein Data Bank structure, a cryo-EM reconstruction of a taxol-stabilized microtubule [64], together with the deposited biological-assembly symmetry operations. All reported P–P distances and angles were evaluated from Cartesian phosphorus coordinates after application of the deposited biological-assembly transformations; the same laboratory z axis was used as the global B_0 direction for every symmetry-generated copy. A single global microtubule axis, common to all 26 assembly operations, was aligned with B_0, consistent with demonstrated electric-field [65] and bundling-based [66] alignment methods. The 5SYF helical assembly has a 9.48 Å rise and a -27.7° rotation per symmetry step. The distance between the alpha- and beta-phosphorus atoms and the angle between the P–P vector and the same global B_0 direction were calculated directly from the coordinates.

Phenomenological decoherence in the BPP picture

For decoherence we retain the BPP functional form but change the interpretation of the correlation time. We model local field fluctuations phenomenologically; equation (6) displays the longitudinal system–bath coupling schematically as

$$\hat{H}_{\mathrm{SB}}(t) = -\sum_i \gamma_i \, \delta B_i(t) \hat{I}_i^z. \tag{6}$$

with two-time correlations

$$\langle \delta B_i(t) \delta B_i(0) \rangle = C_i(0) e^{-|t|/\tau_c}. \tag{7}$$

The corresponding spectral density is the usual Lorentzian

$$\mathscr{J}(\omega) = \frac{2C(0)\tau_c}{1+\omega^2\tau_c^2}. \tag{8}$$

The full BPP model, including transverse fluctuations not written explicitly in equation (6), expresses the longitudinal and transverse relaxation rates as linear combinations of $\mathscr{J}(\omega)$ evaluated at $\omega = 0$, ω_0, and $2\omega_0$, schematically:

$$\frac{1}{T_1} \sim \mathscr{J}(\omega_0) + 4\mathscr{J}(2\omega_0), \tag{9a}$$

$$\frac{1}{T_2} \sim \frac{1}{2}\left[3\mathscr{J}(0) + 5\mathscr{J}(\omega_0) + 2\mathscr{J}(2\omega_0)\right]. \tag{9b}$$

In the liquid-state setting [9], τ_c is identified with the rotational correlation time of ADP tumbling in a liquid. In our cytoskeletal case we keep the same functional dependence but interpret τ_c as the effective correlation time of local field fluctuations at the P sites in the actin/tubulin pocket.

This effective correlation time represents local librations, side-chain motion, water exchange, and lattice vibrations rather than whole-molecule tumbling. The resulting $T_2(\tau_c)$ should be regarded as a phenomenological estimate of the coherence limit imposed by these local fluctuations and can be evaluated over a plausible range of τ_c.

After both the high-field and weak-coupling approximations have been justified, the static Ising interaction is diagonal in the Zeeman basis, and the Hamiltonian can be transformed to the rotating frame. If we restrict ourselves to this Ising-type form (no flip-flop terms $\hat{I}_1^+\hat{I}_2^- + \hat{I}_1^-\hat{I}_2^+$), the eigenstates in the rotating frame are still the computational basis $\{|\uparrow\uparrow\rangle, |\uparrow\downarrow\rangle, |\downarrow\uparrow\rangle, |\downarrow\downarrow\rangle\}$. Consequently, the eigenvalues of our effective Hamiltonian can be directly evaluated using the modified $\Delta\omega_i$ and effective coupling J_{12}^{eff} as follows:

$$\hat{H}|00\rangle = \left[\frac{\Delta\omega_1 + \Delta\omega_2}{2} + \frac{J_{12}^{\text{eff}}}{4}\right]|00\rangle, \tag{10a}$$

$$\hat{H}|01\rangle = \left[\frac{\Delta\omega_1 - \Delta\omega_2}{2} - \frac{J_{12}^{\text{eff}}}{4}\right]|01\rangle, \tag{10b}$$

$$\hat{H}|10\rangle = \left[\frac{-\Delta\omega_1 + \Delta\omega_2}{2} - \frac{J_{12}^{\text{eff}}}{4}\right]|10\rangle, \tag{10c}$$

$$\hat{H}|11\rangle = \left[\frac{-\Delta\omega_1 - \Delta\omega_2}{2} + \frac{J_{12}^{\text{eff}}}{4}\right]|11\rangle. \tag{10d}$$

After establishing the Hamiltonian, eigenstates, and eigenvalues, one can construct the thermal-equilibrium density matrix; calculate the effects of radiofrequency pulses; prepare effective pure and effective Bell states; and apply the Peres-Horodecki criterion to identify entanglement [67]. These steps require pulse design, relaxation dynamics, orientation disorder, and readout mechanisms to be incorporated explicitly into the model. Metrics such as projection, attenuated correlation, and fidelity [68] could then be used to assess quantum-gate implementations and compare theoretical density matrices with experimental measurements.

Pulse sequences related to those described in [9] could be investigated for implementing CNOT, Hadamard, and T gates in cytoskeletal samples. Their feasibility cannot be inferred from the static Hamiltonian alone and requires explicit pulse optimization together with relaxation, orientation-disorder, coupling-network, and readout simulations. Scaling to more complex algorithms, such as Grover search [69], would require larger spectrally distinguishable and selectively addressable spin registers.

Data Availability

The structural coordinates analyzed in this study are publicly available from the RCSB Protein Data Bank under accession codes 7BT7 and 5SYF. No new experimental datasets were generated in this study.

References

1. Feder, J. S. et al. A fluorescent-protein spin qubit. *Nature* **645**, 73–79, https://doi.org/10.1038/s41586-025-09417-w (2025).
2. Ramos-Silva, J.N. et al. A Pulsed Live-Cell Quantum Microscope for Entangled Solid State and Biological Qubits. Preprint at https://arxiv.org/abs/2607.03552 (2026).
3. Fisher, M. P. A. Quantum cognition: the possibility of processing with nuclear spins in the brain. *Annals of Physics* **362**, 593–602, https://doi.org/10.1016/j.aop.2015.08.020 (2015).
4. Yunger Halpern, N. & Crosson, E Quantum Information in the Posner Model of Quantum Cognition. *Annals of Physics* **407**, 92–147, https://doi.org/10.1016/j.aop.2018.11.016 (2019).
5. Agarwal, S., Kattnig, D.R., Aiello, C.D. & Banerjee, A.S The biological qubit: calcium phosphate dimers, not trimers. *J. Phys. Chem. Lett.* **14**, 2518–2525, https://doi.org/10.1021/acs.jpclett.2c03945 (2023).
6. Adams, B., Sinayskiy, I., Agarwal, S. & Petruccione, F Entanglement and Coherence in Pure and Doped Posner Molecules. *Sci Rep* **15**, 12559, https://doi.org/10.1038/s41598-025-96487-5 (2025).
7. Smolin, L Natural and Bionic Neuronal Membranes: Possible Sites for Quantum Biology. Preprint at https://arxiv.org/abs/2001.08522 (2020).
8. Kane, B.E A Silicon-Based Nuclear Spin Quantum Computer. *Nature* **393**, 133–137, https://doi.org/10.1038/30156 (1998).
9. Davino, D.J Quantum Information Processing in Biological Molecules. PhD thesis, Brown U. (2025).

10. Cory, D.G., Fahmy, A.F. & Havel, T.F Ensemble Quantum Computing by NMR Spectroscopy. *Proceedings of the National Academy of Sciences* **94**, 1634–1639, https://doi.org/10.1073/pnas.94.5.1634 (1997).

11. Gershenfeld, N.A. & Chuang, I.L Bulk Spin-Resonance Quantum Computation. *Science* **275**, 350–356, https://doi.org/10.1126/science.275.5298.350 (1997).

12. Knill, E., Chuang, I. & Laflamme, R Effective Pure States for Bulk Quantum Computation. *Phys. Rev. A* **57**, 3348–3363, https://doi.org/10.1103/PhysRevA.57.3348 (1998).

13. Vandersypen, L.M.K., Yannoni, C.S., Sherwood, M.H. & Chuang, I.L Realization of Logically Labeled Effective Pure States for Bulk Quantum Computation. *Phys. Rev. Lett.* **83**, 3085–3088, https://doi.org/10.1103/PhysRevLett.83.3085 (1999).

14. Deutsch, D Quantum Theory, the Church–Turing Principle and the Universal Quantum Computer. *Proc. A* **400**, 97–117, https://doi.org/10.1098/rspa.1985.0070 (1985).

15. Deutsch, D. & Jozsa, R Rapid Solution of Problems by Quantum Computation. *Proceedings: Mathematical and Physical Sciences* **439**, 553–558, https://doi.org/10.1098/rspa.1992.0167 (1992).

16. Smith, S.A. et al. Polyphosphate Exerts Differential Effects on Blood Clotting, Depending on Polymer Size. *Blood* **116**, 4353–4359, https://doi.org/10.1182/blood-2010-01-266791 (2010).

17. Dominguez, R. & Holmes, K.C Actin Structure and Function. *Annu Rev Biophys* **40**, 169–186, https://doi.org/10.1146/annurev-biophys-042910-155359 (2011).

18. Hanson, J. & Lowy, J The Structure of F-Actin and of Actin Filaments Isolated from Muscle. *Journal of Molecular Biology* **6**, 46-IN5, https://doi.org/10.1016/S0022-2836(63)80081-9 (1963).

19. Kumari, A., Kesarwani, S., Javoor, M.G., Vinothkumar, K.R. & Sirajuddin, M Structural Insights into Actin Filament Recognition by Commonly Used Cellular Actin Markers. *EMBO J.* **39**, e104006, https://doi.org/10.15252/embj.2019104006 (2020).

20. Goodson, H.V. & Jonasson, E.M Microtubules and Microtubule-Associated Proteins. *Cold Spring Harb Perspect Biol* **10**, a022608, https://doi.org/10.1101/cshperspect.a022608 (2018).

21. Waites, C., Qu, X. & Bartolini, F The Synaptic Life of Microtubules. *Curr Opin Neurobiol* **69**, 113–123, https://doi.org/10.1016/j.conb.2021.03.004 (2021).

22. Craddock, T. J. A., Hameroff, S.R. & Tuszynski, J.A. The "Quantum Underground": Where Life and Consciousness Originate. In *Biophysics of Consciousness* 459–515 (World Scientific, 2016). https://doi.org/10.1142/9444. ISBN 978-981-4644-25-9.

23. Mavromatos, N.E., Mershin, A. & Nanopoulos, D.V On the Potential of Microtubules for Scalable Quantum Computation. *Eur. Phys. J. Plus* **140**, 1116, https://doi.org/10.1140/epjp/s13360-025-07022-4 (2025).

24. Nishiyama, A., Tanaka, S. & Tuszynski, J.A Waveguide Quantum Electrodynamics: Tryptophans Entangled with Water as Data Qubits in a Microtubule. *Dynamics* **5**, 7, https://doi.org/10.3390/dynamics5010007 (2025).

25. Sahu, S. et al. Atomic Water Channel Controlling Remarkable Properties of a Single Brain Microtubule: Correlating Single Protein to Its Supramolecular Assembly. *Biosensors and Bioelectronics* **47**, 141–148, https://doi.org/10.1016/j.bios.2013.02.050 (2013).

26. Craddock, T. J. A., Friesen, D., Mane, J., Hameroff, S. & Tuszynski, J.A The Feasibility of Coherent Energy Transfer in Microtubules. *J R Soc Interface* **11**, 20140677, https://doi.org/10.1098/rsif.2014.0677 (2014).

27. Babcock, N.S. et al. Ultraviolet Superradiance from Mega-Networks of Tryptophan in Biological Architectures. *J. Phys. Chem. B* **128**, 4035–4046, https://doi.org/10.1021/acs.jpcb.3c07936 (2024).

28. Gassab, L., Pusuluk, O. & Craddock, T.J.A Quantum Information Flow in Microtubule Tryptophan Networks. *Entropy* **28**, 204, https://doi.org/10.3390/e28020204 (2026).

29. Gassab, L. & Craddock, T.J.A Optical Properties of the Cytoskeleton: A Review of Light–Matter Interactions, Quantum Effects, and Biological Implications. *J. Phys. Photonics* **8**, 012006, https://doi.org/10.1088/2515-7647/ae3ee8 (2026).

30. Nishiyama, A., Tanaka, S. & Tuszynski, J.A Quantum Brain Dynamics: Optical and Acoustic Super-Radiance via a Microtubule. *Foundations* **4**, 288–305, https://doi.org/10.3390/foundations4020019 (2024).

31. Craddock, T. J. A., Tuszynski, J.A. & Hameroff, S Cytoskeletal Signaling: Is Memory Encoded in Microtubule Lattices by CaMKII Phosphorylation. *PLOS Computational Biology* **8**, e1002421, https://doi.org/10.1371/journal.pcbi.1002421 (2012).

32. Sahu, S., Ghosh, S., Hirata, K., Fujita, D. & Bandyopadhyay, A Multi-Level Memory-Switching Properties of a Single Brain Microtubule. *Appl. Phys. Lett.* **102**, 123701, https://doi.org/10.1063/1.4793995 (2013).

33. Svitkina, T The Actin Cytoskeleton and Actin-Based Motility. *Cold Spring Harb Perspect Biol* **10**, a018267, https://doi.org/10.1101/cshperspect.a018267 (2018).

34. Sweeney, H.L. & Hammers, D.W Muscle Contraction. *Cold Spring Harb Perspect Biol* **10**, a023200, https://doi.org/10.1101/cshperspect.a023200 (2018).

35. Gibieža, P. & Petrikaitė, V The Regulation of Actin Dynamics during Cell Division and Malignancy. *Am J Cancer Res* **11**, 4050–4069 (2021).

36. May, R.C. & Machesky, L.M Phagocytosis and the Actin Cytoskeleton. *J Cell Sci* **114**, 1061–1077, https://doi.org/10.1242/jcs.114.6.1061 (2001).

37. Burbage, M. & Keppler, S.J Shaping the Humoral Immune Response: Actin Regulators Modulate Antigen Presentation and Influence B-T Interactions. *Mol Immunol* **101**, 370–376, https://doi.org/10.1016/j.molimm.2018.07.026 (2018).

38. Dustin, M.L. & Cooper, J.A The Immunological Synapse and the Actin Cytoskeleton: Molecular Hardware for T Cell Signaling. *Nat Immunol* **1**, 23–29, https://doi.org/10.1038/76877 (2000).

39. Das, S., Mondal, S. & Ghosh, D Carbon Quantum Dots in Bioimaging and Biomedicines. *Front. Bioeng. Biotechnol.* **11**, 1333752, https://doi.org/10.3389/fbioe.2023.1333752 (2024).

40. Niora, M., Mzyk, A. & Berg-Sørensen, K Bio-Sensing with NV-Centers in Diamond. *J. Phys. Photonics* **8**, 012007, https://doi.org/10.1088/2515-7647/ae46fe (2026).

41. Vindolet, B. et al. Sensitive and Quantitative Biosensing Technique Based on NV Centres-Doped Nanodiamonds Applied to Lateral Flow Assays. *Sci Rep* **16**, 7125, https://doi.org/10.1038/s41598-026-37454-6 (2026).

42. Torrado, B., Pannunzio, B., Malacrida, L. & Digman, M.A Fluorescence Lifetime Imaging Microscopy. *Nat Rev Methods Primers* **4**, 80, https://doi.org/10.1038/s43586-024-00358-8 (2024).

43. Huang, H.-W., Yang, S.-L., Huang, C.-C., Chen, Y.-N. & Chen, H.-B Noise-Enhanced Quantum Kernels on Analog Quantum Computers. Preprint at https://arxiv.org/abs/2604.12476 (2026).

44. Rebentrost, P., Mohseni, M., Kassal, I., Lloyd, S. & Aspuru-Guzik, A Environment-Assisted Quantum Transport. *New J. Phys.* **11**, 033003, https://doi.org/10.1088/1367-2630/11/3/033003 (2009).

45. Xin, G., Wang, P. & Jiao, Y Noise-Enhanced Quantum Annealing Approach and Its Application in Plug-in Hybrid Electric Vehicle Charging Optimization. *Electronics Letters* **57**, 314–316, https://doi.org/10.1049/ell2.12112 (2021).

46. Nałęcz-Charkiewicz, K., Charkiewicz, K. & Nowak, R.M Quantum Computing in Bioinformatics: A Systematic Review Mapping. *Brief Bioinform* **25**, bbae391, https://doi.org/10.1093/bib/bbae391 (2024).

47. Baiardi, A., Christandl, M. & Reiher, M Quantum Computing for Molecular Biology. *ChemBioChem* **24**, e202300120, https://doi.org/10.1002/cbic.202300120 (2023).

48. Cudby, J. & Strelchuk, S Nonvariational Quantum Optimisation Approaches to Pangenome-Guided Sequence Assembly. Preprint at https://arxiv.org/abs/2604.06106 (2026).

49. Ghazi Vakili, M. et al. Quantum-Computing-Enhanced Algorithm Unveils Potential KRAS Inhibitors. *Nat Biotechnol* **43**, 1954–1959, https://doi.org/10.1038/s41587-024-02526-3 (2025).

50. Li, J. et al. Quantum Oncology: The Applications of Quantum Computing in Cancer Research. *J Med Syst* **49**, 99, https://doi.org/10.1007/s10916-025-02215-x (2025).

51. Matarèse, B.F.E. & Purushotham, A Quantum Oncology. *Quantum Reports* **7**, 9, https://doi.org/10.3390/quantum7010009 (2025).

52. Matarèse, B.F.E. & Purushotham, A Unlocking Clinical Quantum Oncology through Quantum Control. *European Journal of Cancer* **226**, 115632, https://doi.org/10.1016/j.ejca.2025.115632 (2025).

53. Ramesh, S., Tomesh, T., Riesenfeld, S.J., Chong, F.T. & Pearson, A.T Quantum Computing for Oncology. *Nat Cancer* **5**, 811–816, https://doi.org/10.1038/s43018-024-00770-9 (2024).

54. Santagati, R. et al. Drug Design on Quantum Computers. *Nat. Phys.* **20**, 549–557, https://doi.org/10.1038/s41567-024-02411-5 (2024).

55. Gomase, V.S., Ghatule, A.P., Sharma, R. & Dhamane, S.P Quantum Computing in Drug Discovery Techniques, Challenges, and Emerging Opportunities. *Curr Drug Discov Technol* **23**, e15701638371707, https://doi.org/10.2174/0115701638371707250729040426 (2026).

56. Zhou, Y. et al. Quantum-Machine-Assisted Drug Discovery. *npj Drug Discov.* **3**, 1, https://doi.org/10.1038/s44386-025-00033-2 (2026).

57. Ito, T., Lysenko, A. & Tsunoda, T Optimal Normalization in Quantum-Classical Hybrid Models for Anti-Cancer Drug Response Prediction. Preprint at https://arxiv.org/abs/2505.10037 (2025).

58. Bose, A., Rhrissorrakrai, K., Utro, F. & Parida, L Advancing Single-Cell Omics and Cell-Based Therapeutics with Quantum Computing. *Nat Rev Mol Cell Biol* **27**, 394–408, https://doi.org/10.1038/s41580-025-00918-0 (2026).

59. Nassir, N. et al. Quantum Computing and the Implementation of Precision Medicine. *npj Genom. Med.* **10**, 80, https://doi.org/10.1038/s41525-025-00537-w (2025).

60. Emani, P.S. et al. Quantum Computing at the Frontiers of Biological Sciences. *Nat Methods* **18**, 701–709, https://doi.org/10.1038/s41592-020-01004-3 (2021).

61. Abragam, A. *The Principles of Nuclear Magnetism*. International Series of Monographs on Physics (Oxford University Press, Oxford, New York, 1983). ISBN 978-0-19-852014-6.

62. Slichter, C.P. *Principles of Magnetic Resonance* (Springer Science & Business Media, 2013). ISBN 978-3-662-09441-9.

63. Popp, D., Lednev, V.V. & Jahn, W Methods of Preparing Well-Orientated Sols of f-Actin Containing Filaments Suitable for X-Ray Diffraction. *Journal of Molecular Biology* **197**, 679–684, https://doi.org/10.1016/0022-2836(87)90474-8 (1987).

64. Kellogg, E.H. et al. Insights into the Distinct Mechanisms of Action of Taxane and Non-Taxane Microtubule Stabilizers from Cryo-EM Structures. *J. Mol. Biol.* **429**, 633–646, https://doi.org/10.1016/j.jmb.2017.01.001 (2017).

65. Kim, T., Kao, M.-T., Hasselbrink, E.F. & Meyhöfer, E Active Alignment of Microtubules with Electric Fields. *Nano Lett.* **7**, 211–217, https://doi.org/10.1021/nl061474k (2007).

66. Molodtsov, M.I. et al. A Force-Induced Directional Switch of a Molecular Motor Enables Parallel Microtubule Bundle Formation. *Cell* **167**, 539–552.e14, https://doi.org/10.1016/j.cell.2016.09.029 (2016).

67. Peres, A Separability Criterion for Density Matrices. *Phys. Rev. Lett.* **77**, 1413–1415, https://doi.org/10.1103/PhysRevLett.77.1413 (1996).

68. Fortunato, E.M. et al. Design of Strongly Modulating Pulses to Implement Precise Effective Hamiltonians for Quantum Information Processing. *J. Chem. Phys.* **116**, 7599–7606, https://doi.org/10.1063/1.1465412 (2002).

69. Grover, L.K. A Fast Quantum Mechanical Algorithm for Database Search. In *Proceedings of the 28th Annual ACM Symposium on Theory of Computing (STOC)* 212–219 (Philadelphia, PA, USA, 22–24 May 1996), https://doi.org/10.1145/237814.237866.

70. Scipion, C.P.M. et al. Structural Evidence for the Roles of Divalent Cations in Actin Polymerization and Activation of ATP Hydrolysis. *Proc Natl Acad Sci U S A* **115**, 10345–10350, https://doi.org/10.1073/pnas.1806394115 (2018).

71. Hocky, G.M. et al. Cations Stiffen Actin Filaments by Adhering a Key Structural Element to Adjacent Subunits. *J. Phys. Chem. B* **120**, 4558–4567, https://doi.org/10.1021/acs.jpcb.6b02741 (2016).

72. Menéndez, M., Rivas, G., Díaz, J.F. & Andreu, J.M Control of the Structural Stability of the Tubulin Dimer by One High Affinity Bound Magnesium Ion at Nucleotide N-Site*. *Journal of Biological Chemistry* **273**, 167–176, https://doi.org/10.1074/jbc.273.1.167 (1998).

73. Adams, B. & Petruccione, F Spin Quantum Computing, Spin Quantum Cognition. *Quantum Inf. Process.* **25**, 257, https://doi.org/10.1007/s11128-026-05286-y (2026).

74. Swift, M. W., Van de Walle, C. G. & Fisher, M. P. A. Posner molecules: from atomic structure to nuclear spins. *Phys. Chem. Chem. Phys.* **20**, 12373–12380, https://doi.org/10.1039/C7CP07720C (2018).

75. Weingarten, C.P., Doraiswamy, P.M. & Fisher, M. P. A. A New Spin on Neural Processing: Quantum Cognition. *Front. Hum. Neurosci.* **10**, 541, https://doi.org/10.3389/fnhum.2016.00541 (2016).

76. Gassab, L. et al. Quantum in Biology, Quantum for Biology, and Biology for Quantum: Mapping the Evidence and the Road Ahead. Preprint at https://arxiv.org/abs/2605.00205 (2026).

77. Sholl, C.A A BPP (Bloembergen-Purcell-Pound) Model for Nuclear Spin Relaxation Due to Diffusion in Disordered Systems: Combined Barrier- and Site-Energy Disorder. *J. Phys.: Condens. Matter* **12**, 4285, https://doi.org/10.1088/0953-8984/12/18/313 (2000).

78. Song, Y. et al. Transglutaminase and Polyamination of Tubulin: Posttranslational Modification for Stabilizing Axonal Microtubules. *Neuron* **78**, 109–123, https://doi.org/10.1016/j.neuron.2013.01.036 (2013).

79. Cohn, M. & Hughes, T.R Nuclear Magnetic Resonance Spectra of Adenosine Di- and Triphosphate: II. EFFECT OF COMPLEXING WITH DIVALENT METAL IONS. *Journal of Biological Chemistry* **237**, 176–181, https://doi.org/10.1016/S0021-9258(18)81382-5 (1962).

80. Xu, Q., Huff, L.P., Fujii, M. & Griendling, K.K Redox Regulation of the Actin Cytoskeleton and Its Role in the Vascular System. *Free Radic Biol Med* **109**, 84–107, https://doi.org/10.1016/j.freeradbiomed.2017.03.004 (2017).

81. Milzani, A. et al. The Oxidation Produced by Hydrogen Peroxide on Ca-ATP-G-Actin. *Protein Sci* **9**, 1774–1782, https://doi.org/10.1110/ps.9.9.1774 (2000).

82. Terman, J.R. & Kashina, A Post-Translational Modification and Regulation of Actin. *Curr Opin Cell Biol* **25**, 30–38, https://doi.org/10.1016/j.ceb.2012.10.009 (2013).

83. Herzog, W. & Weber, K In Vitro Assembly of Pure Tubulin into Microtubules in the Absence of Microtubule-Associated Proteins and Glycerol. *Proceedings of the National Academy of Sciences* **74**, 1860–1864, https://doi.org/10.1073/pnas.74.5.1860 (1977).

84. Souza, A.M., Álvarez, G.A. & Suter, D Robust Dynamical Decoupling for Quantum Computing and Quantum Memory. *Phys. Rev. Lett.* **106**, 240501, https://doi.org/10.1103/PhysRevLett.106.240501 (2011).

85. Khodjasteh, K. & Lidar, D.A Fault-Tolerant Quantum Dynamical Decoupling. *Phys. Rev. Lett.* **95**, 180501, https://doi.org/10.1103/PhysRevLett.95.180501 (2005).

86. Viola, L., Knill, E. & Lloyd, S Dynamical Decoupling of Open Quantum Systems. *Phys. Rev. Lett.* **82**, 2417–2421, https://doi.org/10.1103/PhysRevLett.82.2417 (1999).

87. Uhrig, G.S Keeping a Quantum Bit Alive by Optimized π-Pulse Sequences. *Phys. Rev. Lett.* **98**, 100504, https://doi.org/10.1103/PhysRevLett.98.100504 (2007).

88. de Lange, G., Wang, Z.H., Ristè, D., Dobrovitski, V.V. & Hanson, R Universal Dynamical Decoupling of a Single Solid-State Spin from a Spin Bath. *Science* **330**, 60–63, https://doi.org/10.1126/science.1192739 (2010).

89. Maurer, P.C. et al. Room-Temperature Quantum Bit Memory Exceeding One Second. *Science* **336**, 1283–1286, https://doi.org/10.1126/science.1220513 (2012).

90. Dolde, F. et al. Room-Temperature Entanglement between Single Defect Spins in Diamond. *Nature Phys* **9**, 139–143, https://doi.org/10.1038/nphys2545 (2013).

91. Cai, J., Retzker, A., Jelezko, F. & Plenio, M.B A Large-Scale Quantum Simulator on a Diamond Surface at Room Temperature. *Nature Phys* **9**, 168–173, https://doi.org/10.1038/nphys2519 (2013).

92. Neumann, P. et al. Quantum Register Based on Coupled Electron Spins in a Room-Temperature Solid. *Nature Phys* **6**, 249–253, https://doi.org/10.1038/nphys1536 (2010).

93. Waldherr, G. et al. Quantum Error Correction in a Solid-State Hybrid Spin Register. *Nature* **506**, 204–207, https://doi.org/10.1038/nature12919 (2014).

94. Kalb, N. et al. Entanglement Distillation between Solid-State Quantum Network Nodes. *Science* **356**, 928–932, https://doi.org/10.1126/science.aan0070 (2017).

95. Neumann, P. et al. Single-Shot Readout of a Single Nuclear Spin. *Science* **329**, 542–544, https://doi.org/10.1126/science.1189075 (2010).

96. Kehayias, P. et al. Solution Nuclear Magnetic Resonance Spectroscopy on a Nanostructured Diamond Chip. *Nat. Commun.* **8**, 188, https://doi.org/10.1038/s41467-017-00266-4 (2017).

97. Jakobi, I. et al. Measuring Broadband Magnetic Fields on the Nanoscale Using a Hybrid Quantum Register. *Nat. Nanotechnol.* **12**, 67–72, https://doi.org/10.1038/nnano.2016.163 (2017).

Funding

This research was supported by the Canada Research Chairs Program (CRC-2022-00204) and the University of Waterloo. L.G. acknowledges support from the University of Waterloo Provost's Program for Interdisciplinary Postdoctoral Scholars.

Author Contributions

Conceptualization, R.T. and T.J.A.C.; methodology, R.T., L.G. and T.J.A.C.; formal analysis, R.T. and L.G.; investigation, R.T.; writing—original draft preparation, R.T., L.G. and T.J.A.C.; writing—review and editing, R.T., L.G. and T.J.A.C.; supervision, T.J.A.C.; funding, T.J.A.C. All authors have read and agreed to the published version of the manuscript.

Competing Interests

The authors declare no competing interests.